



**HAL**  
open science

## Single and multiphase CFD approaches for modelling partially baffled stirred vessels: comparison of experimental data with numerical predictions

Jean-Philippe Torr , D. F. Fletcher, Thierry Lasuye, Catherine Xuereb

### ► To cite this version:

Jean-Philippe Torr , D. F. Fletcher, Thierry Lasuye, Catherine Xuereb. Single and multiphase CFD approaches for modelling partially baffled stirred vessels: comparison of experimental data with numerical predictions. *Chemical Engineering Science*, 2007, 62 (22), pp.6246-6262. 10.1016/j.ces.2007.06.044 . hal-00707690

**HAL Id: hal-00707690**

**<https://hal.science/hal-00707690>**

Submitted on 1 Mar 2022

**HAL** is a multi-disciplinary open access archive for the deposit and dissemination of scientific research documents, whether they are published or not. The documents may come from teaching and research institutions in France or abroad, or from public or private research centers.

L'archive ouverte pluridisciplinaire **HAL**, est destin e au d p t et   la diffusion de documents scientifiques de niveau recherche, publi s ou non,  manant des  tablissements d'enseignement et de recherche fran ais ou  trangers, des laboratoires publics ou priv s.



## Open Archive Toulouse Archive Ouverte (OATAO)

OATAO is an open access repository that collects the work of Toulouse researchers and makes it freely available over the web where possible.

This is an author-deposited version published in: <http://oatao.univ-toulouse.fr/>  
Eprints ID : 3013

**To link to this article :**

URL : <http://dx.doi.org/10.1016/j.ces.2007.06.044>

To cite this version: Torr , Jean-Philippe and Fletcher, David F. and Lasuye, T. and Xuereb, Catherine ( 2007) *Single and multiphase CFD approaches for modelling partially baffled stirred vessels: comparison of experimental data with numerical predictions*. Chemical Engineering Science, Vol. 62 (n 22 ). pp. 6246-6262. ISSN 0009-2509

Any correspondence concerning this service should be sent to the repository administrator: [staff-oatao@inp-toulouse.fr](mailto:staff-oatao@inp-toulouse.fr)

# Single and multiphase CFD approaches for modelling partially baffled stirred vessels: Comparison of experimental data with numerical predictions

Jean-Philippe Torr <sup>a,b,c</sup>, David F. Fletcher<sup>b,\*</sup>, Thierry Lasuye<sup>c</sup>, Catherine Xuereb<sup>a</sup>

<sup>a</sup>Universit  de Toulouse, Laboratoire de G nie Chimique CNRS/INP/UPS, Toulouse, France

<sup>b</sup>School of Chemical and Biomolecular Engineering, The University of Sydney, NSW 2006, Australia

<sup>c</sup>LVM Quality and Innovation Department, Usine de Mazingarbe, Chemin des Soldats, 62160 Bully Les Mines, France

---

## Abstract

Whilst the use of CFD to study mixing vessels is now common-place, there are still many specialised applications that are yet to be addressed. Here we present CFD and PIV results for a hydrodynamic study of a partially baffled vessel with a free surface. The standard  $k-\epsilon$  and SSG Reynolds Stress turbulence models are used and the numerical predictions of the mean flow field are compared with experimental data for single phase modelling. At low rotation rates a flat free surface is observed and the flow is simulated using a single phase model, whilst at high rotation rates an Eulerian–Eulerian multiphase model is used to capture the free surface location, even under conditions when gas is drawn down to the impeller. It is shown that there are significant transient effects that mean many of the “rules of thumb” that have been developed for fully baffled vessels must be revisited. In particular such flows have central vortices that are unsteady and complex, transient flow-induced vortical structures generated by the impeller–baffle interactions and require a significant number of simulated agitator rotations before meaningful statistical analysis can be performed. Surprisingly, better agreement between CFD and experimental data was obtained using the  $k-\epsilon$  than the SSG Reynolds stress model. The multiphase inhomogeneous approach used here with simplified physics assumptions gives good agreement for power consumption, and with PIV measurements with flat and deformed free surfaces, making this affordable method practical to avoid the erroneous modelling assumption of a flat free surface often made in such cases.

*Keywords:* Partially baffled vessel; Mixing; Free surface; Vortex; Turbulence model; CFD; PIV

---

## 1. Introduction

Mixing is one of the most common and most important operations in the process industries. The situation most frequently encountered in industry is an agitated vessel which is fully baffled, causing the destruction of the impeller-generated vortex and thus having a flat liquid surface. The category of systems represented by stirred baffled tanks that are equipped with baffles but where the baffling effect is not sufficient to prevent vortex formation are called partially baffled systems. Although partially baffled reactors are frequently encountered in the polymer, pharmaceutical and specialty chemicals industries, they have been poorly studied in the literature, where there is a lack

of experimental and numerical studies. As a consequence, the study of the hydrodynamics which develops in these stirred tanks, where the free surface deformation cannot be neglected, is particularly interesting and challenging.

Extensive literature reviews of experimental and CFD simulation work have been provided for fully baffled vessels (see Brucato et al., 1998; Van den Akker, 2006), with a great number of these works concentrated on turbulent, single phase flows in tanks stirred by Rushton turbines. In addition, most experimental studies have been carried out with the liquid surface covered by a lid to prevent vortex formation. The unbaffled case, in comparison with the baffled case, has been studied less. Few studies were found in the literature that relate to the computation of a turbulent flow in a stirred vessel, including free surface deformation. Ciofalo et al. (1996) presented numerical simulations of the free surface profile for unbaffled tanks agitated by a Rushton turbine and a paddle impeller. The authors

developed an iterative method, used with a treatment of non-orthogonal body fitted grids, which allowed prediction of the vortex shape. This was found to be in good agreement with Nagata's (1975) theory and with vortex height experiments conducted in a model tank. In other papers, an interface capturing scheme based on the volume-of-fluid (VOF) method, reported by Hirt and Nichols (1981), was used to predict the free surface shape. Serra et al. (2001) simulated a wavy free surface for a baffled CSTR using VOF in a fully transient simulation of the flow field. Haque et al. (2006) carried out numerical simulation of the turbulent flow with a free surface vortex in unbaffled vessels agitated by a paddle impeller and a Rushton turbine. Their simulations showed that the free surface could be captured well using the standard VOF method available in ANSYS CFX but their cases resulted in smooth, parabolic-shaped interfaces and no entrainment of gas into the impeller swept region. In addition, they compared results from the SST and SSG Reynolds stress models and obtained slightly better agreement between measured and simulated tangential velocity fields with the Reynolds stress model. A more detailed review of simulations of unbaffled and partially baffled vessels can be found in a previous paper by Torré et al. (2007a).

Various turbulence models have already been tested and compared for mixing vessel computational studies by several authors. The standard  $k-\varepsilon$  model (Launder and Spalding, 1974) has served the engineering community well for many years because it is robust, rapid and provides reasonable results for many flows (Paul et al., 2004). This model, which uses the eddy viscosity hypothesis, is known to over-estimate turbulent viscosities in stagnant areas and may have limitations for systems with high streamline curvature, swirling flows or vortex generation, as mentioned in Alcamo et al. (2005), Ciofalo et al. (1996) and Jenne and Reuss (1999). Jaworski et al. (1997), who studied the flow generated by a Rushton turbine with a sliding mesh approach using the standard  $k-\varepsilon$  and RNG  $k-\varepsilon$  turbulences models, concluded that the mean velocity components predicted with the two models did not differ significantly in the whole tank and matched the experimental data well, except in the trailing vortex region. In addition, the same author (Jaworski and Zakrzewska, 2002) compared the CFD predictions of the mean velocity and the turbulent kinetic energy obtained by using six different turbulence models, with experimental data from LDA. The models used were the standard  $k-\varepsilon$ , the RNG  $k-\varepsilon$ , the realizable  $k-\varepsilon$ , the Chen–Kim  $k-\varepsilon$ , the optimised Chen–Kim  $k-\varepsilon$  and a Reynolds Stress Model. The best results were obtained using the standard  $k-\varepsilon$  model which gave good predictions for the mean velocity but a significant under-prediction of the turbulent kinetic energy (Jaworski and Zakrzewska, 2002).

It would be expected that more accurate numerical results would be obtained through the use of models not based on the assumption of an isotropic eddy viscosity. The Algebraic Stress Model (ASM) was used by Armenante et al. (1997), but the Reynolds Stress Models (RSM) has not been widely used for mixing vessels applications due to the frequent convergence problems encountered, as explained by Aubin et al. (2004). More fundamental approaches, such as LES and DNS, are

discussed in a recent review by Van den Akker (2006) but these are generally too expensive for engineering applications. In this study, both the standard  $k-\varepsilon$  eddy viscosity model and the second moment Reynolds Stress Model, developed by Speziale et al. (1991), Basara and Younis (1995) and denoted RSM-SSG, have been tested for single phase flows.

In a previous paper, it was demonstrated that a steady, Eulerian–Eulerian multiphase method can predict the vortex shape in good agreement with experimental data for different agitator rotation speeds (Torre et al., 2007a). In addition, the same method was applied in Torre et al. (2007b) to compute the free surface shape evolution during agitator stopping. However, no comparisons between the flow-field predictions and experimental data were reported. In the first part of this study guidelines on the simulation procedures required to obtain meaningful mean velocity data are obtained using single phase simulations for a case where the surface is flat. The single phase predicted results are then compared with results from the inhomogeneous multiphase flow model. Then, the capability of the numerical methods used to capture the free surface shape and the hydrodynamics of partially baffled systems are examined through comparisons between experimental observations and PIV results.

## 2. Experimental apparatus

The stirred tank investigated is a partially baffled pilot reactor, equipped with a three bladed retreat curve bottom-entering impeller and two beaver-tail baffles. The agitator is a copy of a real industrial design used in suspension polymerisation reactors. This model is derived from the classical retreat curve impeller (RCI) but with larger blades. Note the industrial agitator is glass-coated and has smoother surfaces than the steel model used here but it is not expected that this would change the results significantly. The stirred vessel was specially designed to allow particle image velocimetry (PIV) measurements in geometries found in real industrial applications. The cylindrical vessel is placed inside a transparent square tank filled with deionised water in order to minimise shell curvature and refraction problems at the cylindrical surface of the inner vessel. The use of another fluid instead of water for matching the refractive index of the glass (Budwig, 1994) is not necessary for the experimental apparatus used in this study as the curvature radius of the vessel shell is sufficiently large to avoid high refraction effects, and a simple calibration using water was sufficient. A torque transducer (HBM GmbH, T5 model, 20 Nm of nominal torque) located on the agitator shaft, coupled to a measuring amplifier (SCOUT55 from HBM GmbH) enabled the measurement of the impeller torque to be made. The precision of the torque measurements is  $\pm 0.1$  Nm in the range of 0–20 Nm. The mixing vessel and the agitator used are presented in Fig. 1 and all the geometrical dimensions are summarised in Table 1.

The flow in the stirred vessel was investigated using the PIV technique. The principles of PIV have been covered in many papers and therefore the reader is referred to Adrian (1991), La Fontaine and Shepherd (1996), Willert and Gharib (1991) for details and Mavros (2001) for a review of the subject.

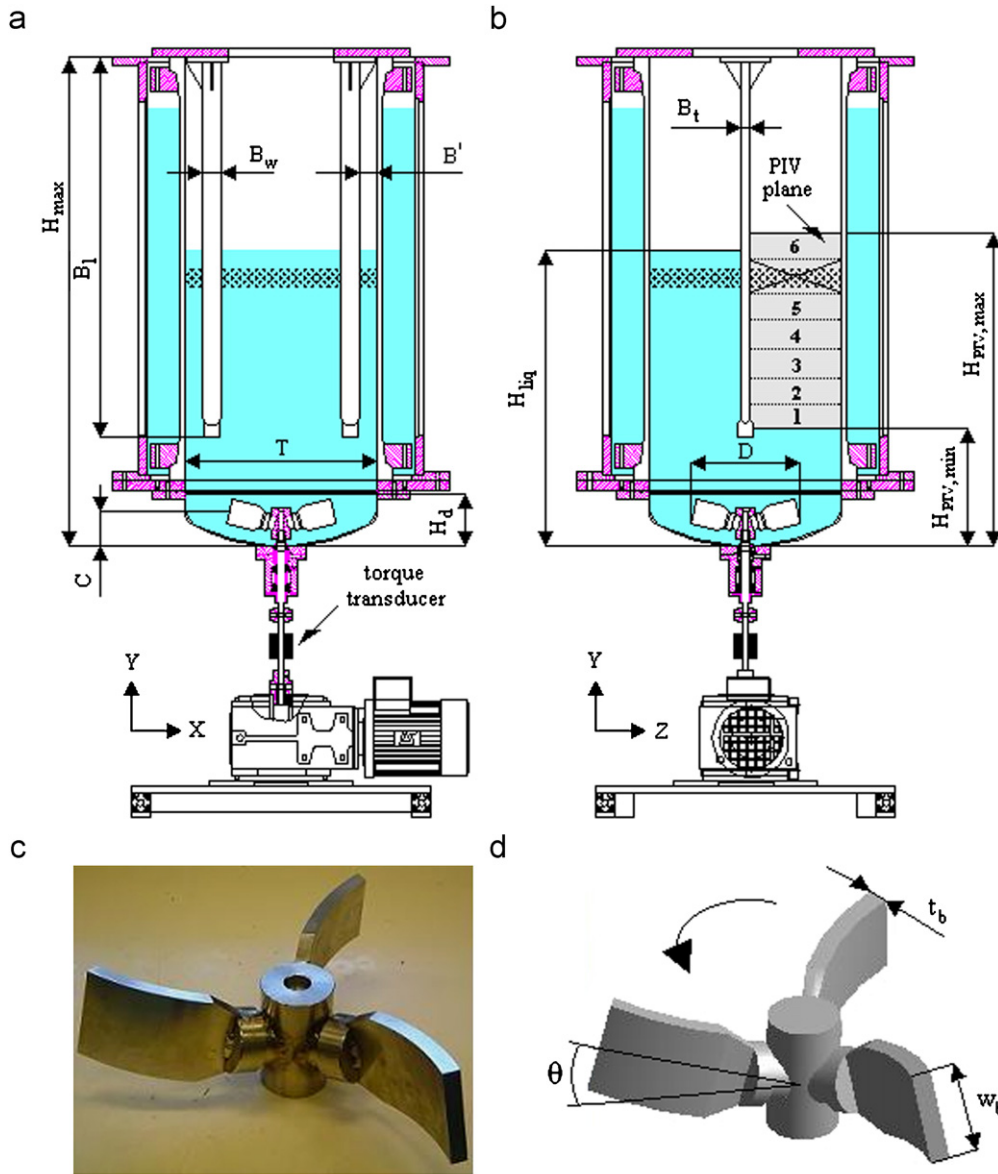


Fig. 1. (a)  $XY$  view of the mixing vessel; (b)  $YZ$  view of the mixing vessel; (c) picture of the agitator; (d) CFD model and details of the agitator.

The instantaneous velocity fields were measured in the agitated vessel described above, filled with 1091 of tap water for all experiments.

The flow was seeded with fluorescent tracer particles of Rhodamine-B provided by Microparticles GmbH (excitation/emission wavelengths: 575 nm/584 nm, fluorochromes incorporated in a PMMA matrix,  $1 \mu\text{m} < \text{diameter} < 20 \mu\text{m}$ ). A double pulsed Milite Nd:YAG continuum laser of wavelength 532 nm (green) was used to illuminate these particles with a short time difference ( $\Delta t = 1$  and  $0.4$  ms for  $N = 100$  and  $200$  RPM, respectively). An appropriate lens and optical system allowed transformation of the laser beam into a vertical laser sheet of 100 mm height and about 1 mm thickness passing through the centre of the vessel and midway between the two baffles.

To capture the frames exposed by laser pulses, a black and white CCD camera (La Vision Imager Intense) with a resolution of  $1376 \times 1024$  pixels<sup>2</sup> was used. The camera was equipped with a telephoto lens (Nikon–Nikkor 50 mm/1.2) that was used to focus on the laser sheet. It was located 1087 mm away from the light sheet and normal to the jacket sidewall. A high pass filter was placed in front of the camera which enabled capture of light with a wavelength greater than 550 nm, protecting the CCD sensor from unwanted light reflections on gas bubbles and improving contrast. A timing controller was used to link and synchronise the laser and the camera. The image acquisition rate was set to 3 Hz in order not to freeze the flow in the event that low frequency instabilities exist. The snapshots were not synchronised with the passage of impeller blades.

Table 1  
Dimensions of the agitated vessel studied

	Symbol	Value
Tank diameter	$T$	450 mm
Maximum tank height	$H_{\max}$	1156 mm
Bottom dish height	$H_d$	122.9 mm
Agitator diameter	$D$	260 mm
Number of agitator blades	$n_b$	3
Agitator blade width	$w_b$	58 mm
Agitator blade thickness	$t_b$	9 mm
Agitator retreat angle	$\theta$	15°
Agitator clearance	$C$	47.2 mm
Baffles length	$B_l$	900 mm
Number of baffles	$n_B$	2
Baffle width	$B_w$	46 mm
Baffle thickness	$B_t$	27 mm
Distance baffle-shell	$B'$	38.5 mm
Initial liquid height	$H_{liq}$	700 mm
Bottom height of the PIV plane	$H_{PIV,\min}$	278 mm
Top height of the PIV plane	$H_{PIV,\max}$	738 mm

The images were processed using the Davis software package with interrogation cell sizes of 64 pixels for the preliminary step and 32 pixels with 50% overlap for the final step. The concentration of seeded particles was adjusted to have between 5 and 10 particles in each  $32 \times 32$  pixels<sup>2</sup> interrogation window. The most probable particle displacement is calculated using a FFT based cross-correlation function to obtain a velocity vector for the considered interrogation window. A radial-axial instantaneous velocity vector map over the whole target area was produced by repeating the cross-correlation for each interrogation area. In each case, 960 images were found to be necessary and sufficient to obtain the averaged flow field.

To cover the entire half tank, the measurements required the construction of a mosaic composed of six different sectors included in the PIV plane, as shown in Fig. 1. Each sector measures 80 mm vertically, which is smaller than the dimension of the laser sheet (100 mm) to allow optimal intensity in the considered area. Horizontally, each sector covered the entire half tank (225 mm). The sectors were adjusted vertically on specific  $Y$  coordinates to allow 10 mm of superimposition of two adjacent sectors, thus making a junction area. In each junction area, the velocity value considered for the velocity field was the result of the arithmetic average of the two velocities coming from the two adjacent sectors. The discrepancy in the velocity magnitude between the values measured at the same locations in adjacent fields of view and the averaged value in the junction areas was typically less than 10% for the axial and radial velocities along the entire vessel radius. An exception was the radial velocities measured close to the vessel axis ( $r < 50$  mm) where the discrepancy between the average value and the velocity measured in each sector was up to 50%. This relatively high difference is attributed to the very low value of the radial velocity near the vessel axis, combined with the uncertainties resulting from the transient effects in this area caused by rising bubbles and a precessing vortex. An irregular glass welding around the vessel led to significant light distortions and made

it impossible to obtain reliable data acquisition in the vicinity of  $Y = 633$  mm. Thus, the area from  $Y = 609$  mm to 658 mm has not been considered, as shown in Fig. 1.

Two different cameras were used for experimental data capture. The vorticity filaments were filmed using a high resolution CMOS camera (HCC-1000 model from VDS Vosskuhler) monitored by the NV1000 software from New Vision Technologies. The image resolution was  $1024 \times 1024$  pixels<sup>2</sup>. The camera was located normal to the vessel jacket sidewall, and was equipped with a telephoto lens (Nikon-Nikkor 50 mm/1.2). The capture of the precessing vortex moving on the free surface required the mounting of a camera above the free surface. For these measurements, the video data acquisition was made using a commercial Webcam (Philips Toucam Pro II), equipped with a CDD sensor, linked to a standard PC. The data were transferred to the computer via a USB link and the frame rate was 15 frames/s.

### 3. CFD modelling

Numerical simulations of the turbulent flow field have been carried out using the commercial CFD package ANSYS-CFX 10.0. The predictions were made in a fully transient manner using fluids at 25 °C and the well-known sliding mesh approach. The flow fields obtained from the computations need to be averaged in time for comparison with the PIV data. This process has highlighted several important questions concerning the time required before averaging can be started and how many agitator rotations are necessary to obtain relevant numerical data. The answers to these questions have proved to be complex and are discussed later.

Single phase simulations with water only and a flat free surface were run initially to understand certain elements of the problem before multiphase simulations were run. The governing equations and the turbulence closure models used in the single phase simulations are presented in Appendix A.

The multiphase simulations were carried out using an Eulerian-Eulerian multiphase model which considers the water and air as the continuous and the dispersed phases, respectively. The modelling of the free surface deformation by using a gas/liquid inhomogeneous approach appeared to be a good solution as shown by the results obtained in earlier papers which used an MRF approach and a steady-state assumption (Torré et al., 2007a) and a transient simulation for a decreasing agitator speed (Torré et al., 2007b). In this inhomogeneous approach, a set of continuity and momentum equations for each phase were coupled with a homogeneous  $k-\varepsilon$  turbulence model. This choice of the novel numerical approach used here, rather than a homogenous flow model together with a VOF approach, is required because as well as a free surface, there is gas entrained into the impeller region. If a VOF model were used there would be no way for the gas to disengage from the liquid and unphysical results would be obtained. The equation system, based on the resolution of the Reynolds Averaged continuity and Navier-Stokes equations, is solved in a transient manner with assumptions of a constant drag coefficient ( $C_D = 0.44$ ) and a single bubble diameter,  $d_b$ , of 3 mm. The

basis for choosing these parameters is presented in Torr  et al. (2007a). In short, they are used to specify a drag force between that gas and liquid phases that is of the correct size to allow gas separation to occur at a physically sensible rate. There is no attempt to model the detailed multi-scale physics of bubble formation and agglomeration behaviour as this is not the aim of the current work but rather we have used these parameters to obtain a free surface profile that matches experimental data. The model equations and the assumptions used for modelling of the free surface are not repeated here as they are detailed in previous papers Torr  et al. (2007a,b).

The stirred vessel was modelled using an unstructured grid of 230,000 and 209,000 nodes (958,000 and 832,000 elements) for the single and multiphase cases, respectively, optimised by sensitivity studies to be fine enough to capture the flow without being excessive, and to give grid independent velocity fields (Torr  et al., 2007a,b). The rotating domain was set to be the entire bottom dish which includes the agitator and the sliding interface was represented by the horizontal surface which connects the cylindrical part of the vessel and the bottom dish. A no-slip condition was applied to all walls (vessel and bottom dish walls, agitator and baffles) except at the very top surface of the vessel where the free-slip condition was set. This boundary condition prevents any flow through the surface and sets the normal gradients for all other quantities to zero, representing a lid that is well removed from the region containing liquid. The simulations were carried out with an initial liquid height of 700 mm, and for the inhomogeneous approach with 100 mm of gas above the liquid interface. The quantities of liquid and gas remain fixed in the simulation and the initial condition described above is used to enable the water to rise up the vessel walls as the vortex is generated with no liquid loss from the computational domain.

The simulations were run using the sliding mesh approach using the transient rotor-stator model available in ANSYS CFX 10.0, with a 2° rotation angle of the agitator per time-step and a maximum of 10 coefficient loops at each time-step, which ensured good convergence. The transient runs were initialised from steady-state results obtained using the multiple reference frame (MRF) approach. The instantaneous velocity of the liquid was monitored during the simulation at 15 monitor points located on the vertical median plane of the two baffles. These monitor points were located vertically at three different vessel heights ( $Y = 200, 400$  and  $600$  mm) and radially at five positions which are  $r = 0, \pm 75$  and  $\pm 150$  mm.

## 4. Results

### 4.1. Transient instabilities and quasi-steady state

Fig. 2 presents the computed velocity field obtained using the  $k-\epsilon$  turbulence model at nine of the monitoring-points versus the number of agitator rotations for  $N = 100$  RPM. The velocities measured on the monitor points where  $r < 0$  were found to have the same tendencies as those for  $r > 0$ . Thus, to simplify the figure, only the monitor points with  $r \geq 0$  are presented.

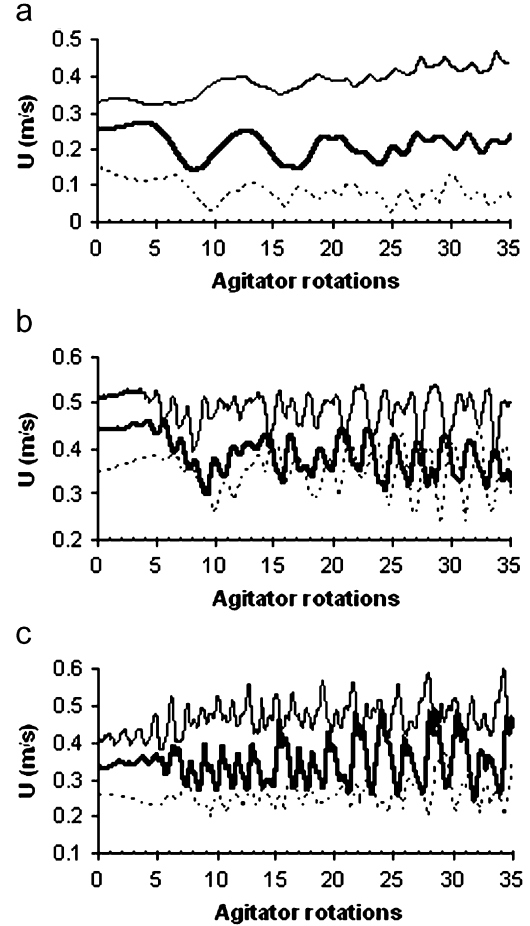


Fig. 2. Instantaneous velocity evolution versus number of agitator rotations for different locations in the vessel and  $N = 100$  RPM. Regular line:  $Y = 200$  mm; bold line:  $Y = 400$  mm; dashed line:  $Y = 600$  mm. (a)  $r = 0$ ; (b)  $r = 75$  mm; (c)  $r = 150$  mm.

Although the normalized residuals of the momentum, continuity and turbulence equations were all below  $10^{-4}$ , the evolution of the velocity during the first 15 agitator rotations ( $N_r < 15$ ) differs from the following rotations ( $N_r > 15$ ). For  $0 < N_r < 5$ , the velocity remains quasi-stable with weak oscillations. For  $5 < N_r < 15$ , a pronounced decrease, followed by an increase of the velocity magnitude for the points located at  $r = 0$  and  $75$  mm is observed, while this variation is less pronounced for  $r = 150$  mm. The reproducibility of the velocity profiles has been tested on two different simulations and it was found to be exactly the same. Thus, the initial agitator rotations were not included in the averaging process and the collection of transient statistics was started only after 15 revolutions.

The number of agitator revolutions needed to reach a quasi-steady state in our study is of the same order of magnitude as the number of revolutions needed by Li et al. (2004, 2005) to reach a quasi-steady state. Their numerical studies of a mixing vessel equipped with a retreat curve impeller and only one cylindrical baffle were carried out using a sliding mesh approach, the shear stress transport turbulence model and used a steady-state result as initialisation, required 9–10 agitator rotations to reach the quasi-steady state. In contrast, Campolo et al. (2002)

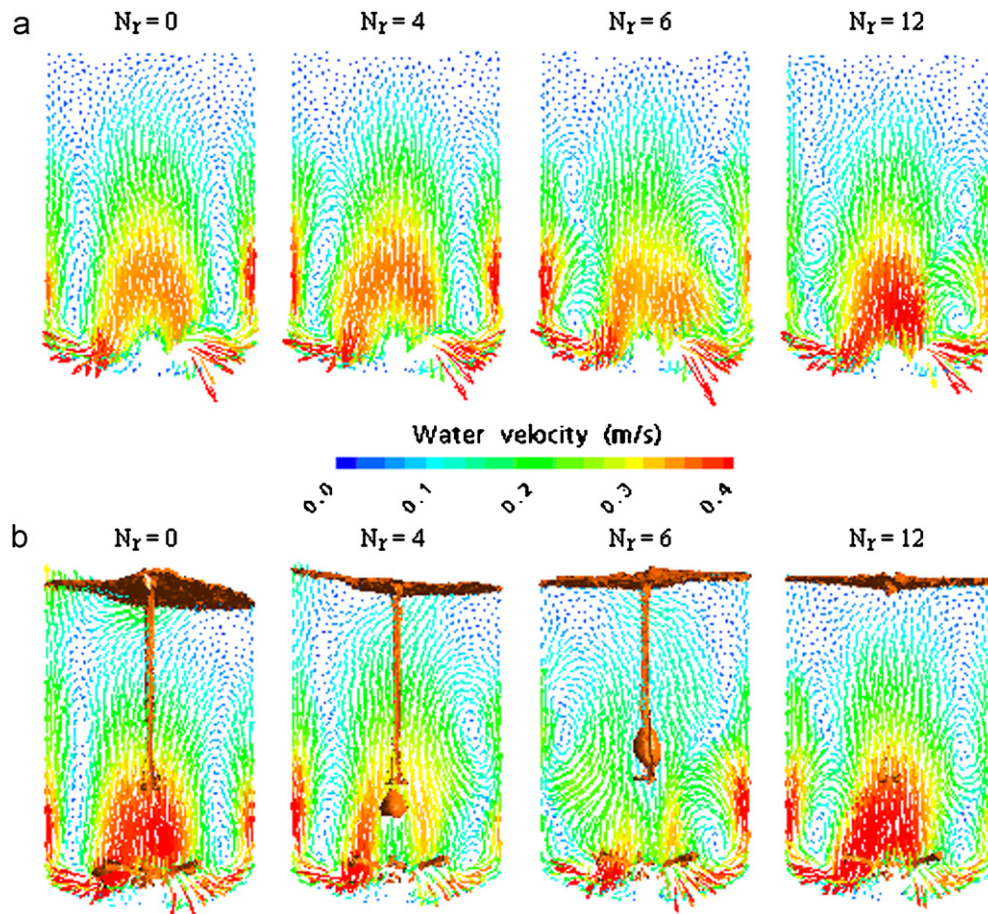


Fig. 3. Axial–radial instantaneous velocity vectors on the vertical median plane of the two baffles obtained after steady-state ( $N_r = 0$ ) and at the end of  $N_r = 4, 6$  and  $12$  agitator revolutions,  $N = 100$  RPM: (a) single phase simulation; (b) two phase simulation.

ran their simulations during 30–40 agitator revolutions because they started their sliding mesh computations from conditions of a stationary fluid. As concluded also by Li et al. (2005), the use of a converged steady-state result as initialisation of a transient sliding mesh run greatly reduces the number of agitator revolutions needed before a quasi-steady state is reached.

Single phase simulations run in steady-state mode (SS) lead to good convergence (residuals  $< 10^{-4}$ ). Contrary to this, the multiphase runs do not converge as well (residuals between  $10^{-4}$  and  $10^{-3}$ ) when the agitator rotation speed was set to a value below 200 RPM. As shown in Fig. 3(b), the free surface shape predicted by the inhomogeneous model for  $N = 100$  RPM starts off by being deformed at  $N_r = 0$  due to the poor convergence of the steady-state initialisation but flattens out after a few impeller revolutions.

The predicted flat free surface at 100 RPM is in very good agreement with the experimental observations made at this rotation speed. Fig. 3 shows that the steady-state initialisation imposes a double loop flow structure and it takes about five revolutions to break it into multiple secondary recirculation loops. In addition, a fast fourier transform (FFT) spectral analysis (Duhamel and Vetterli, 1990) of the numerical velocity data obtained from monitor points during many agitator revolutions showed a complex, periodic flow structure. The number

of acquisition points compatible with this FFT analysis must be a power of two and was set to  $Z = 2048$  and  $4096$  for the  $k-\epsilon$  and SSG simulations, respectively. These data were sampled numerically each iteration with a frequency,  $F_s$ , equal to 300 Hz, giving the resolution frequencies ( $\Delta f = F_s/Z_{FFT}$ ) equal to 0.15 and 0.073 Hz for the  $k-\epsilon$  and SSG spectral analysis, respectively. The power spectra obtained at  $N = 100$  RPM, using the  $k-\epsilon$  and the SSG turbulence models, are presented in Fig. 4(a) and (b) for one example position, respectively ( $Y = 200$  mm and  $r = 75$  mm). The frequency analysis revealed comparable characteristic frequencies which are 0.73, 1.32 Hz with the  $k-\epsilon$  model and 0.95, 1.46 Hz for the SSG model. The three-bladed agitator frequency is 5 Hz which corresponds to three times the complete revolution frequency of the agitator at 100 RPM (1.66 Hz). Thus the intrinsic period of the flow was found not to be an exact multiple of the agitator rotation rate. These periodic fluctuations of the flow can be linked to instabilities.

The investigation of macro instabilities (MIs) in stirred vessels has received much attention by numerous authors. MIs are principally caused by changes in the circulation patterns which constrains the flow to oscillate between different stable configurations, and to one (or more) precessing vortices revolving around the axis of the tank. In the investigations carried out by

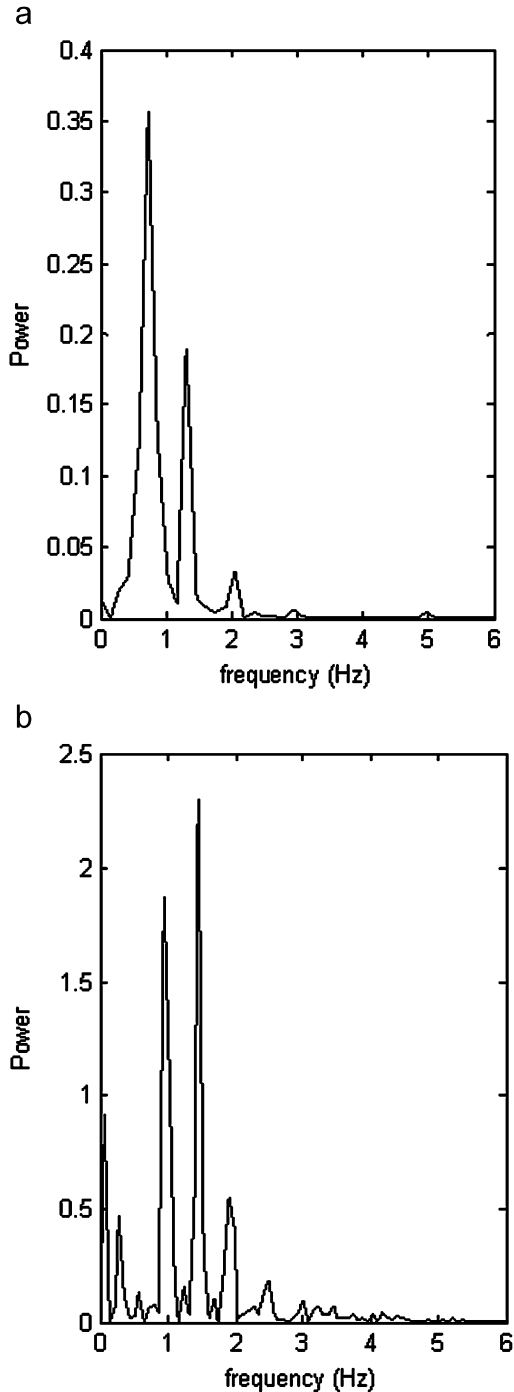


Fig. 4. Fast Fourier transform power spectrum of the velocity;  $Y = 200$  mm,  $r = 75$  mm,  $N = 100$  RPM; (a)  $k-\epsilon$  model, (b) Reynolds Stress (SSG) model.

Hasal et al. (2000), Nikiforaki et al. (2003, 2004), Roussinova et al. (2003) and more recently Ducci and Yianneskis (2007) and Paglianti et al. (2006), the reader can find further details on the subject. In the partially baffled stirred vessel investigated in this study, a small camera (Philips Toucam ProII) located just above the liquid surface on the vessel axis allowed tracking of the free surface deformations. A precessing vortex, revolving around the vessel axis with an estimated frequency of 0.4 Hz, is clearly visible at 100 RPM and an actual trajectory is shown in

Fig. 5. The flow instabilities deduced from the computational analysis cannot be linked to the precessing vortex phenomena observed experimentally because the free surface effects are not taken into account in the single phase simulations. Nevertheless, the experimental measurements of free surface behaviour must be pointed out for the system studied. Although we were not able to correlate the predicted frequencies to any agitator-baffles interaction, a period of around two rotations appeared to be the most characteristic, as shown in an analysis of vorticity structures detailed in the next section.

#### 4.2. Vorticity structures

Fig. 6(a) presents the  $10\text{ s}^{-1}$  vorticity isosurface, obtained numerically at  $N = 100$  RPM with the single phase approach using the standard  $k-\epsilon$  turbulence model, coloured by the water velocity to highlight the high and low velocity areas. It shows a high vorticity region in the middle of the tank extending from above the agitator to the free surface. When the circumferential velocity is sufficiently high in this region to deform the free surface, a central vortex is formed. The most interesting and unusual feature is the evidence of a swirling vortical structure with filamentous connections of vortices between the rear of the two baffles and the agitator region. These filaments rotate in the vessel in the same direction as the agitator but the global movement was found to have a period of about two agitator revolutions. These vortical structures cannot be observed experimentally with a camera at low rotation speed but they are highlighted at higher rotation speed because they trap and carry gas bubbles. As shown in Fig. 6(b) at 217 RPM, a vortical filament which contains gas bubbles links the rear of the baffle and the bottom dish area then rotates in the vessel. This swirling movement which develops with a relative low frequency leads to locally high and low velocity values giving oscillations of the local velocity values, explaining the features observed in Fig. 2. This vortical structure confirms the characteristic frequencies obtained by FFT and provides further evidence of the flow complexity which exists in this partially baffled system.

#### 4.3. Numerical predictions versus experimental data

For the numerical results, the data have been averaged only over the fifteenth to thirtieth revolutions from the single phase and multiphase cases for the reasons outlined earlier. These numerical predictions have been compared with experimental observations and PIV measurements at two rotations speeds (100 and 200 RPM).

##### 4.3.1. Effect of the turbulence model

The single phase model has been used at low rotation speed ( $N = 100$  RPM) with the flat free surface hypothesis for investigating the effect of the turbulence models on the prediction of the velocity profiles. Fig. 7 shows a comparison between experimental data and numerical predictions ( $N = 100$  RPM) of axial and radial velocities along the entire vessel radius

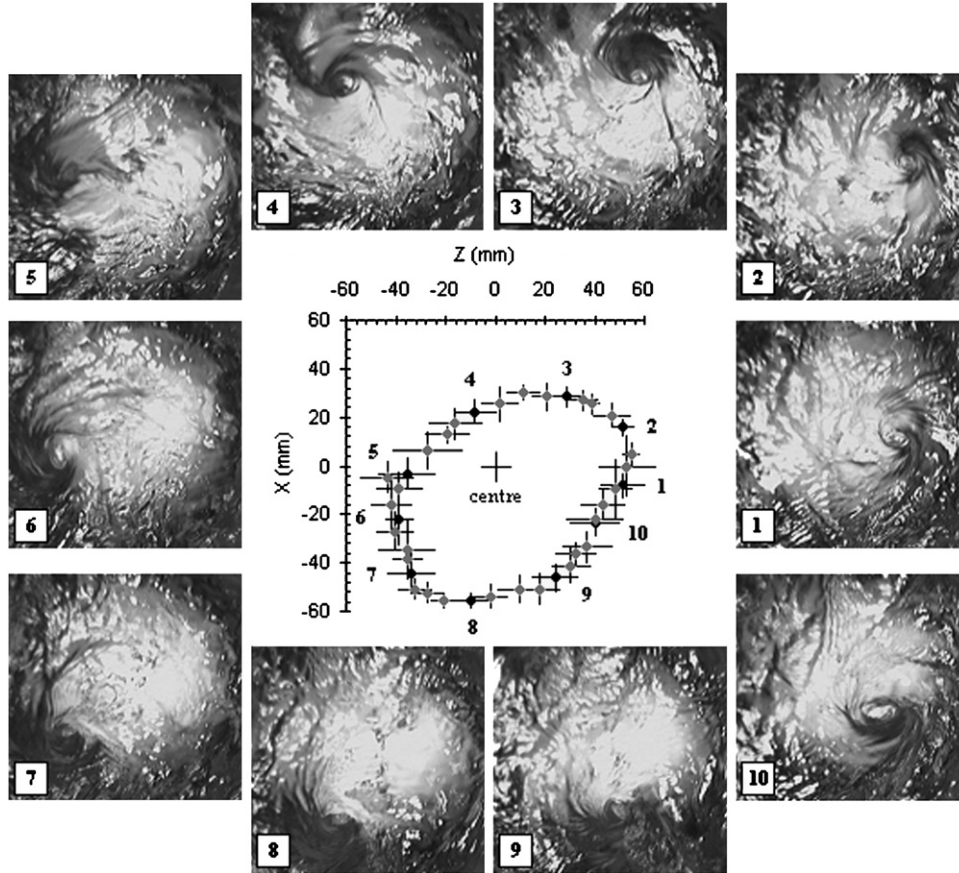


Fig. 5. Snapshots of the precessing vortex visible on the free surface ( $N = 100$  RPM) and trajectory around the vessel axis; the  $Z$  direction is in the plane orthogonal to the baffles;  $X$  direction in the baffle plane; the centre is located on the vessel axis.

corresponding to three vessel heights of  $Y = 318, 458$  and  $598$  mm from the bottom dish, obtained using the  $k-\epsilon$  and the SSG Reynolds stress turbulence models.

Firstly, it can be noted that there is good agreement for the axial velocity as shown in Fig. 7. The  $k-\epsilon$  turbulence model provides numerical predictions close to the experimental data and in better agreement than data obtained using the RSM-SSG model. Moderate agreement between experimental and numerical results was observed with the radial velocity component for both turbulence models tested. The reasons for the deviations observed between experimental and computational results relative to the radial velocity could be linked both to the computational method and to the experimental strategy.

On one hand, the numerical data have been averaged successively during the agitator rotations to observe how the average develops and it was noted that a stable result was never reached during the averaging process and the velocity changes because of the periodic nature of the flow. For example, the fluctuation of the averaged velocity from revolution 22 to 30 numerically estimated on the line of  $Y = 388$  mm with the  $k-\epsilon$  model is  $\pm 0.015$  and  $\pm 0.02$  m/s for the axial and radial velocity components, respectively (the error bars corresponding to these fluctuations have been dropped from the figure for clarity). Thus, the accuracy of the prediction of the very low radial velocity component is strongly affected by

the instantaneous velocity fluctuations impacting substantially on the numerical averaged result.

On the other hand, due to the small magnitude of the radial velocity compared with the axial and tangential ones, the experimental measurement of this velocity component could be affected by any small non-alignment or asymmetry of the experimental apparatus, as well as by a slight deviation of the laser plane. An asymmetry linked to the position of the laser sheet (e.g. vertical alignment, radial position different from zero) has been studied using the CFD results obtained at 100 RPM. Instead of considering the orthogonal baffle plane as the PIV plane, the numerical velocity fields have been plotted on planes inclined at  $\pm 5^\circ$  and  $\pm 10^\circ$  to the original plane. These do not show the same level of asymmetry on the axis as measured experimentally. A small intrinsic geometrical asymmetry of the vessel (small errors in the vertical alignment of the baffles, or different baffle-shell distances) or one induced by the agitator rotation (e.g. different interaction with the two suspended baffles) could be present. Unfortunately, these asymmetric effects could not be quantified experimentally.

In addition, it must be pointed out that the gas bubble disengagement, observed experimentally near the vessel axis, has a major impact on the liquid velocity in this region. The disengagement process of the gas pumped down near the axis generates radial motion of the bubbles which entrains liquid.

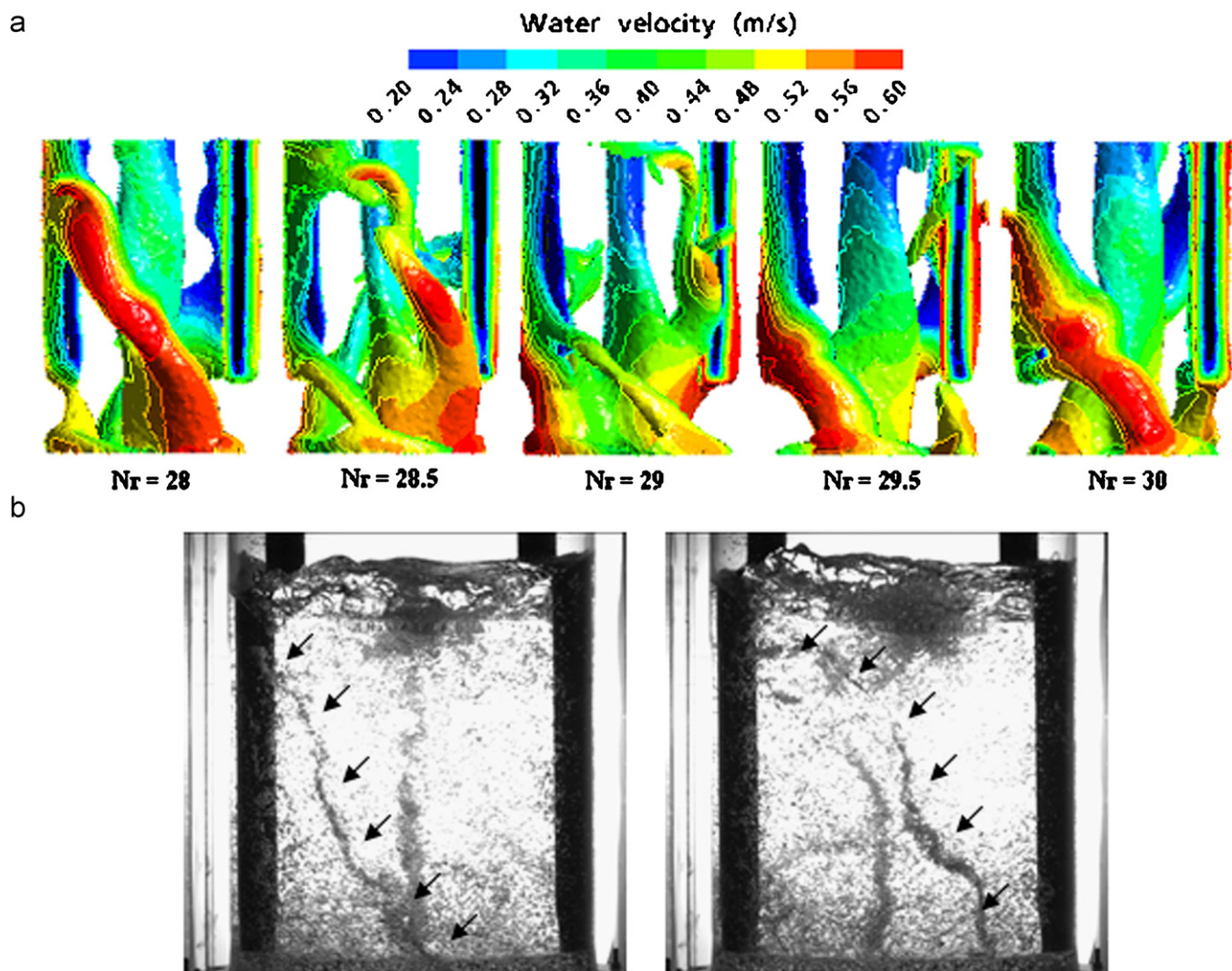


Fig. 6. (a) Numerical isosurface of vorticity equal to  $10\text{ s}^{-1}$  for the time period covered from the 28th to 30th agitator rotations obtained using a single-phase simulation and the  $k-\varepsilon$  turbulence model ( $N=100$  RPM), coloured by a contour plot of water velocity; (b) two successive experimental snapshots at  $N=217$  RPM.

This effect modifies the liquid flow patterns imparted by the impeller and cannot be predicted using the CFD model used here, as it is not designed to model the details of the bubble disengagement process. Finally, the motion of the precessing vortex could also affect the velocity values measured near the free surface. The vortex core, as shown previously, revolves in a volume which is contained inside a 100 mm diameter cylinder around the vessel axis (including the most eccentric trajectories), may explain the deviation observed in this area. We return to this point in Section 4.3.4.

More globally, the numerical time-averaged contour plots of the normalised axial velocity  $U_a^*$  ( $=U_a/U_{\text{tip}}$ ), obtained at 100 RPM with the  $k-\varepsilon$  model and the SGG Reynolds stress model shown in Fig. 8(b) and (c), are compared with PIV experimental data plotted in Fig. 8(a). In the same way, the normalised axial-radial velocity  $U_{ar}^*$ , defined as  $U_{ar}^* = (U_a^2 + U_r^2)^{0.5}/U_{\text{tip}}$  which is the projected norm of the velocity vectors on the plane orthogonal to the baffles is also presented in

Figs. 9(b) and (c) and is compared with the experimental data of Fig. 9(a) obtained at  $N = 100$  RPM. The “onion-skin” shapes of the axial and axial-radial velocity contours, as well as their values (velocity magnitudes) are in good agreement with the PIV data for the  $k-\varepsilon$  model over the entire domain corresponding to the PIV plane. Surprisingly, the modelling using the SGG Reynolds Stress model leads to characteristic shapes of the velocity contours close to the vessel axis which differ significantly from those obtained experimentally and those predicted using the  $k-\varepsilon$  model. The predictions close to the vessel wall are in good agreement with experimental data for both the turbulence models tested. The Reynolds Stress model used, which is known to provide more accurate results for high swirling flows such as those encountered in unbaffled vessels for example, is not superior to the standard  $k-\varepsilon$  model for our situation. Thus, the  $k-\varepsilon$  model appears to be well adapted and to perform better than the RSM-SSG for this case and has therefore been chosen as the turbulence model for developing the multiphase approach.

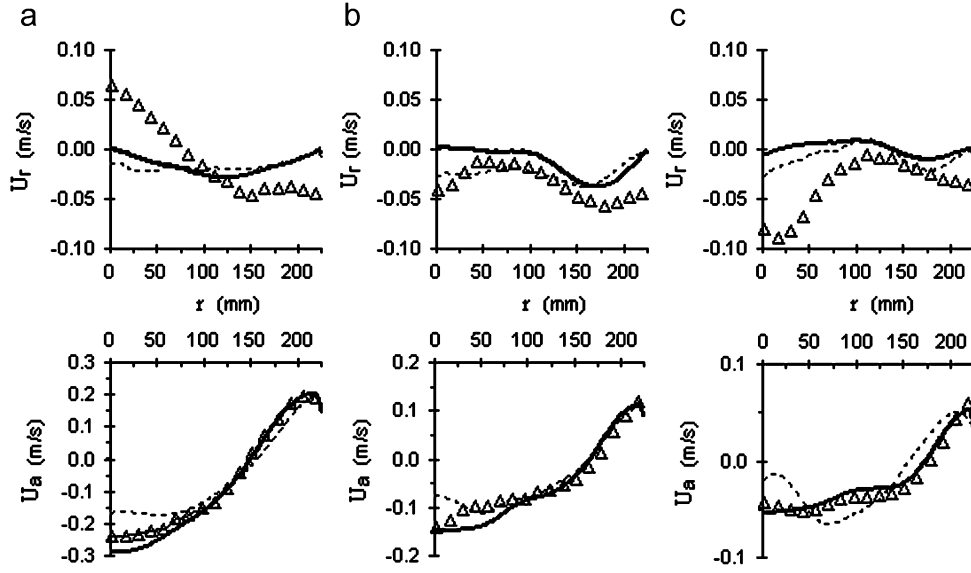


Fig. 7. Comparisons between radial/axial velocity measurements obtained by PIV and CFD predictions at different heights ( $N = 100$  RPM); symbols: PIV; bold line: CFD with the  $k-\epsilon$  model; dashed line: CFD with the Reynolds Stress (SSG) model; (a)  $Y = 318$  mm; (b)  $Y = 458$  mm; (c)  $Y = 598$  mm.

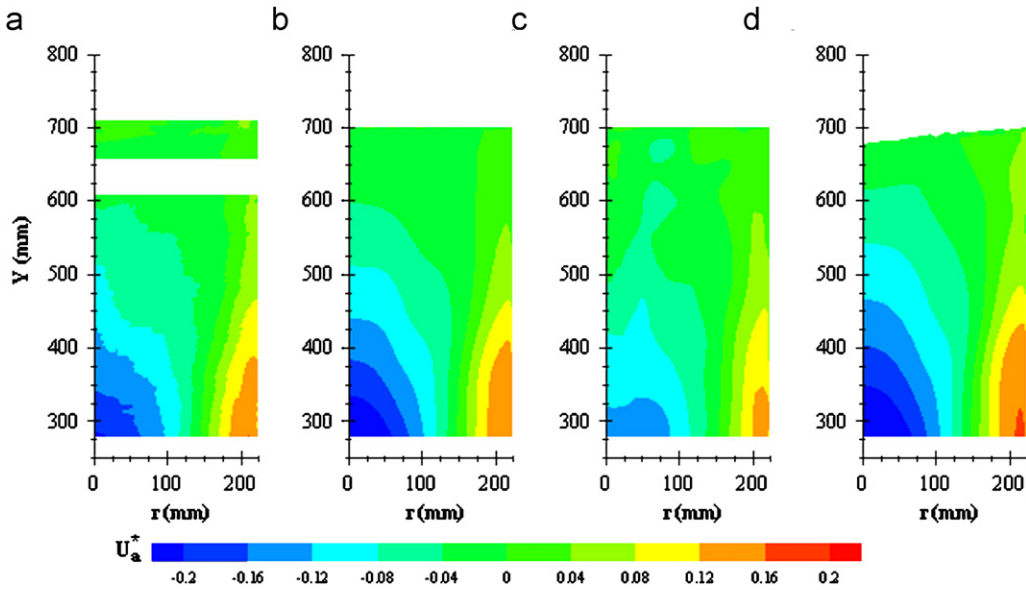


Fig. 8. Contours plots of normalised axial velocity on the PIV plane for  $N = 100$  RPM: (a) experimental PIV data; (b) single phase numerical data using the  $k-\epsilon$  model; (c) single phase numerical data using the Reynolds Stress (SSG) model; (d) multiphase numerical data using the  $k-\epsilon$  model.

#### 4.3.2. Single phase versus multiphase modelling approaches

Fig. 8(d) and 9(d) present contour plots of normalised axial velocity and axial-radial velocity obtained using the multiphase approach. The numerical results have been averaged over agitator revolutions fifteen to thirty. The results presented are the liquid phase velocities below the free surface, characterised by an isosurface of averaged liquid volume fraction equal to 0.9. The free surface location obtained by averaging the liquid volume fraction during fifteen agitator revolutions is predicted to have a maximum deformation of only 25 mm at the centre tank. This result is in agreement with experimental observations that give a quasi-flat free surface at

this rotation speed, although the small precessing vortex which revolves around the vessel axis was not predicted numerically. In addition, the comparisons between Figs. 8(a) and (d), and then Figs. 9(a) and (d), show that the axial velocity and the axial-radial velocity fields are in good agreement with both the PIV results and the single phase numerical predictions. This is an important result as it shows that taking the free surface deformation into account in the simulations using an inhomogeneous approach does not modify the results obtained from a single phase simulation at low rotation speed. The simplest case of a flat free surface is solved in good agreement with experimental data by the complex inhomogeneous approach.

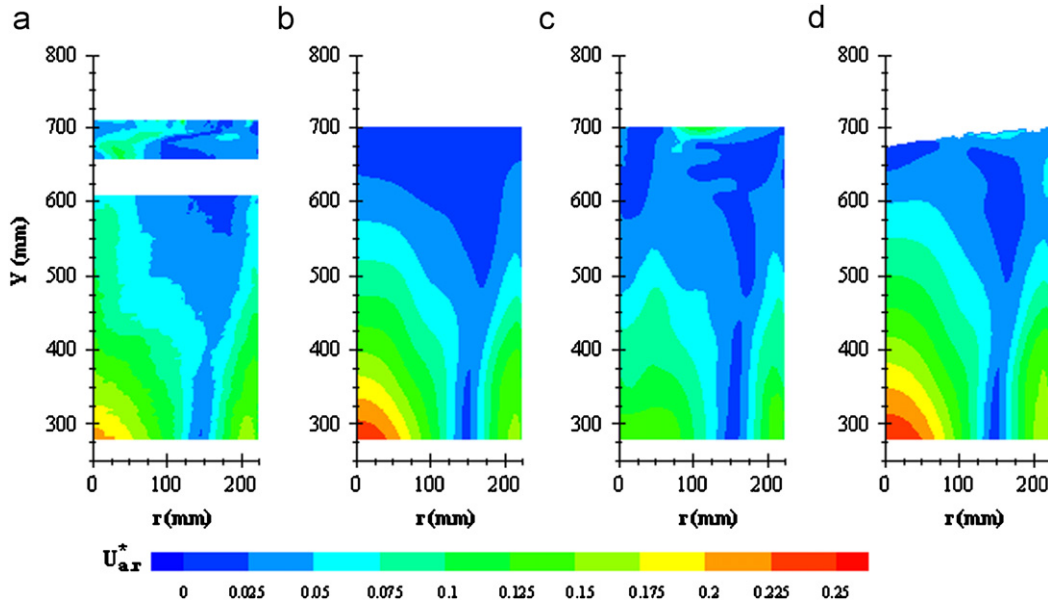


Fig. 9. Contours plots of normalised axial–radial velocity on the PIV plane for  $N = 100$  RPM: (a) experimental PIV data; (b) single phase numerical data using the  $k-\epsilon$  model; (c) single phase numerical data using the Reynolds Stress (SSG) model; (d) multiphase numerical data using the  $k-\epsilon$  model.

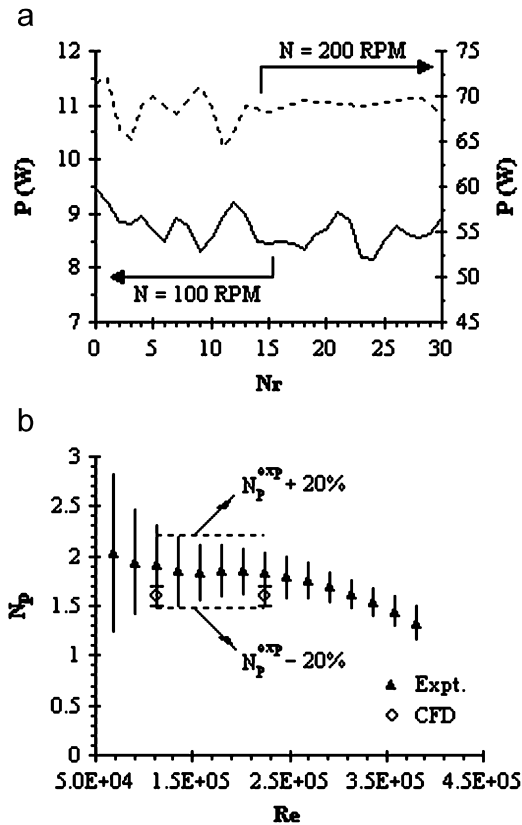


Fig. 10. (a) Simulated power consumption versus number of agitator revolutions for  $N = 100$  and  $200$  RPM. (b) Experimental and computed power number versus Reynolds number.

#### 4.3.3. Power consumption

The power consumption was calculated as the product of the torque  $T_0$  on the agitator and shaft, with the impeller angular velocity equal to  $2\pi N$  ( $N$  in  $s^{-1}$ ). Fig. 10(a) shows the evolution

of the power input predicted using the inhomogeneous approach versus the number of agitator revolutions for  $N = 100$  RPM and  $200$  RPM. For  $N = 200$  RPM, the power consumption stabilises, while some fluctuations persists for  $N = 100$  RPM after 15

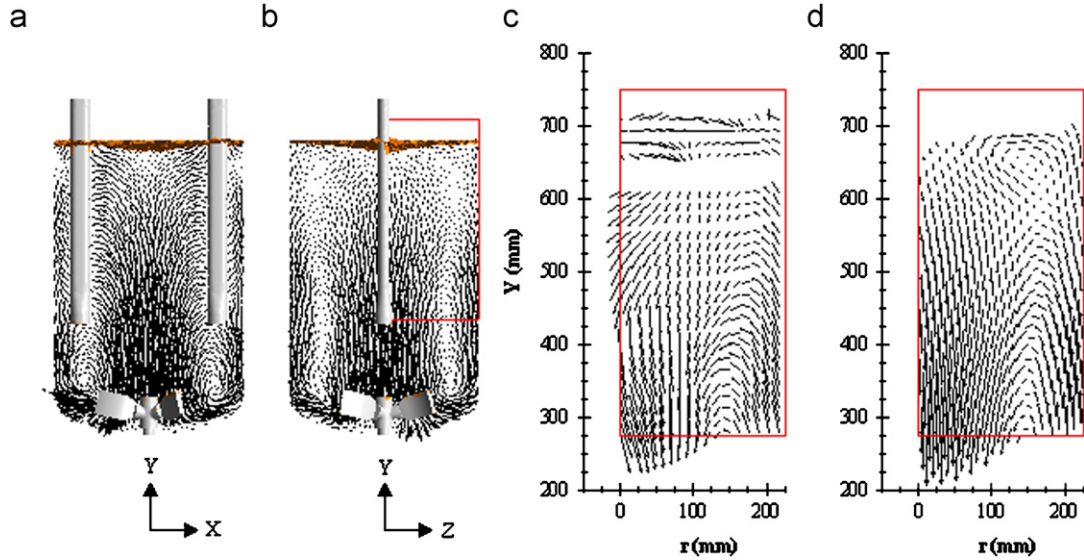


Fig. 11. Numerical axial-radial velocity vectors for  $N = 100$  RPM on the  $XY$  baffle plane (a) and on the  $YZ$  plane orthogonal to baffles (b); zoom of the velocity vector field on the PIV plane: (c) experimental; (d) numerical.

agitator rotations. These fluctuations are due to transitions in the structure of the flow field and have previously been observed in the transient simulations carried out by Campolo et al. (2002) in a study of a similar partially baffled vessel. These results are consistent with the analysis of the instantaneous velocity fields made earlier in this paper, where the quasi-steady state was deemed to be reached after 15 agitator rotations.

The power draw can be also expressed in turbulent flow as  $P = N_p \rho N^3 D^5$ , where  $N_p$  is the dimensionless power number of the impeller. For the agitator used in this study, no power data are available from the literature. The torque has been measured from  $N = 60$  to 340 RPM, corresponding to Reynolds numbers from  $6.7 \times 10^4$  to  $3.8 \times 10^5$ , respectively. Sufficient data are necessary to calculate the power number due to the torque fluctuations caused by the unsteady nature of the flow. For each rotation speed, the torque has been recorded during 2 min at 5 Hz (120 instantaneous values) to obtain the arithmetic average of the torque and its standard deviation ( $\sigma$ ). The absolute error attached to the averaged torque is obtained by adding the measurement precision uncertainty (0.1 Nm) to  $2\sigma$  (to give a 95% confidence interval).

The experimental data for the averaged power numbers are presented in Fig. 10(b) versus the Reynolds number. The uncertainty of the torque measurement is very high at low velocity and the power numbers obtained for  $Re < 1.1 \times 10^5$  are not considered in the following analysis. For  $Re \geq 2.5 \times 10^5$  ( $N > 220$  RPM), the power number decreases with increasing Reynolds number, due to the vortex formation, and the significant vessel aeration observed visually at high rotation speed. Verschuren et al. (2000) have reported exactly the same evolutionary behaviour of the power number versus  $Re$  and come to the same conclusions regarding the impact of the vortex at high Reynolds number ( $Re > 10^5$ ). For  $1.1 \times 10^5 \leq Re \leq 2.2 \times 10^5$  ( $100 \text{ RPM} \leq N \leq 200 \text{ RPM}$ ), the power number is stable and its averaged value  $N_p^{\text{exp}}$  is equal to  $1.85 \pm 0.4$ .

In addition, the power number has been calculated numerically using the torque values from the CFD simulations at 100 and 200 RPM. The averaged value of the power number obtained from the fiftieth to the thirtieth agitator revolutions were the same for 100 and 200 RPM, which is consistent with a constant value of  $N_p$  in turbulent flow without aeration. The uncertainty has been taken to be two times the standard deviation of the power number values obtained at 100 RPM from  $15 \leq Nr \leq 30$ . The power number predicted numerically was  $N_p^{\text{CFD}} = 1.6 \pm 0.1$ . The numerical predictions have been compared with the experimental values in Fig. 10(b) and fairly good agreement is shown.

#### 4.3.4. Hydrodynamics with flat and deformed free surfaces

At  $N = 200$  RPM, a vortex is created at the free surface and the assumption of a flat free surface cannot be made (Torré et al., 2007a). Due to the presence of only two beaver-tail baffles in the vessel, the baffling effect is not sufficient to prevent the high tangential fluid motion and a vortex is formed. Its shape can be predicted numerically with the inhomogeneous approach and allows the velocity field to be captured accurately in cases with a deformed free surface.

The numerical velocity fields are compared with PIV data through vector fields in Figs. 11 and 12. As presented in Fig. 11(a) and 11(b) for  $N = 100$  RPM, and in Figs. 12(a) and 12(b) for  $N = 200$  RPM, the global mixing action is based on a typical circulation consisting of a downward stream in the centre of the vessel and an upward stream at the periphery, with a rotational flow superposed on these streams. For the two agitator speeds, the velocity vectors show that the impeller generates a radial fluid jet that is deflected by the curved dish in the upward direction and generates the upward flow. The agitation pumps the liquid axially in the centre of the vessel, causing a large circulation loop to be created between the

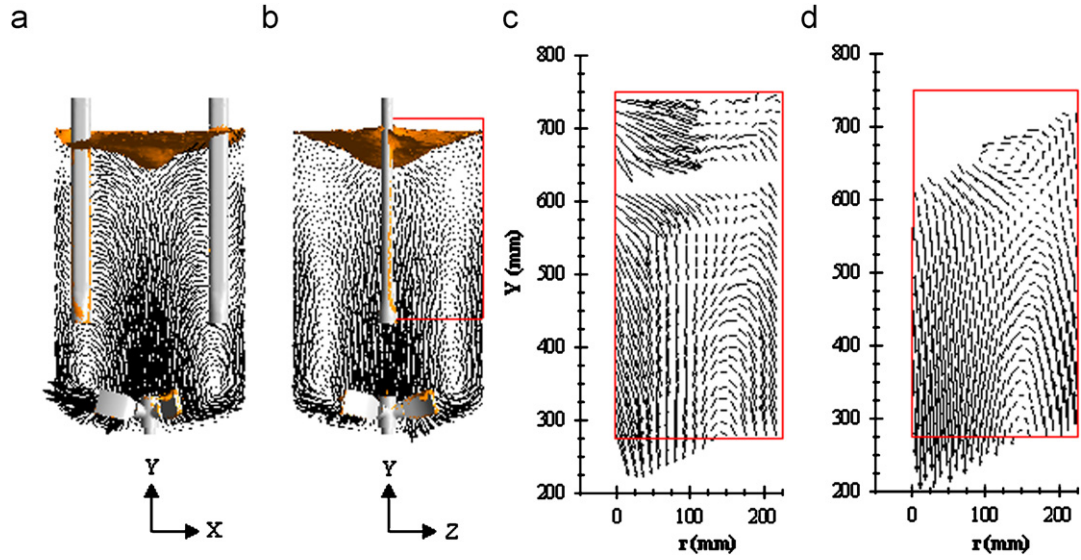


Fig. 12. Numerical axial-radial velocity vectors for  $N = 200$  RPM on the  $XY$  baffle plane (a) and on the  $YZ$  plane orthogonal to the baffles (b); zoom of the velocity vector field on the PIV plane; (c) experimental; (d) numerical.

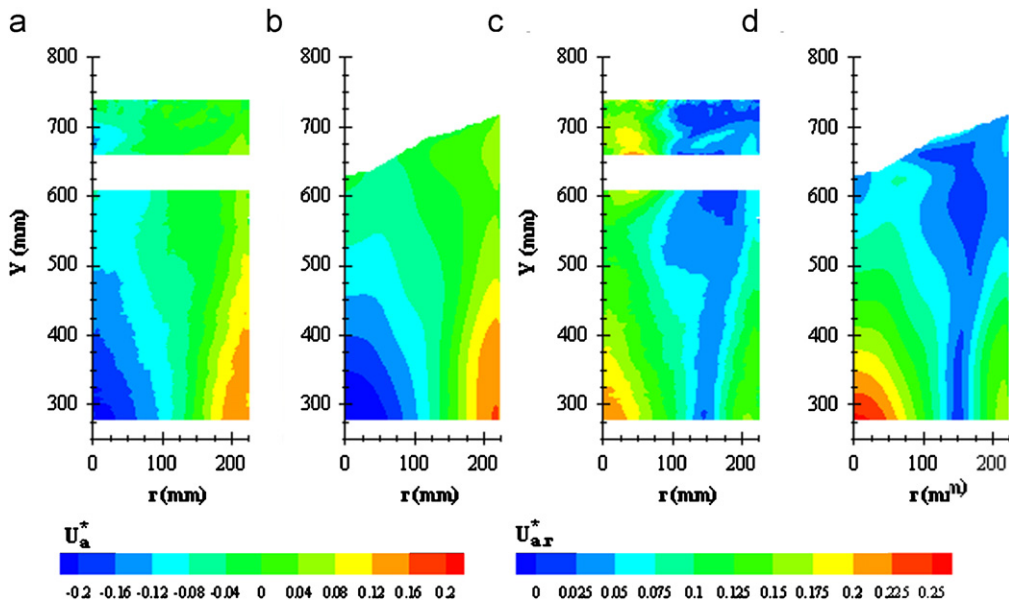


Fig. 13. Contours plots of normalised velocity on the PIV plane for  $N = 200$  RPM: (a) experimental axial velocity; (b) numerical axial velocity; (c) experimental axial-radial velocity; (d) numerical axial-radial velocity.

vessel axis and the vessel wall. It should be noted that a small recirculation loop is formed below each baffle.

The non-zero value of the radial velocity measured on the vessel axis at  $N = 100$  RPM and already pointed out in the analysis of Fig. 7, is discussed here through the analysis of the experimental axial-radial vector field presented in Fig. 11(c). The velocity patterns differ from those obtained at higher agitator rotation speeds by a negative radial velocity of the liquid in the area  $r < 100$  mm and  $Y > 425$  mm. This unusual feature of the flow is assumed to be due to the movement of the precessing vortex coupled with the disengagement of gas bubbles in this area. At 100 RPM, the aeration point is not located at

the vessel axis as observed for higher rotation speeds but follows the precessing vortex movement, which rotates around the vessel axis along a circular path with a maximum diameter of 100 mm. This assumption is corroborated by the high radial component of the vectors obtained inside the vortex core located in the top left corner of the PIV plane shown in Fig. 12(c) for  $N = 200$  RPM. The extreme instability of the vortex shape leads to the presence of both liquid and gas in the measurement area corresponding to the location of vortex core and leads to the measurement of a liquid velocity in the vortex core. Therefore, a measurement point is sometimes in the liquid and sometimes in the gas, which leads to spurious vectors as the free surface

is deformed and unstable. The experimental data show a non-zero radial component of the velocity vectors along and close to the vessel axis. It can be hypothesized that, at this rotation speed, the effect of air introduction at the bottom of the vortex core and the disengagement of these gas bubbles before reaching the agitator due to buoyancy, contributes to add a radial component to the velocity measured close to the vessel axis. In Fig. 12 these vectors are present in the vortex core at 200 RPM. This is unusual when compared with the results obtained with an unbaffled vessel, where no liquid is present inside the vortex core due to the development of a stable free surface shape that generates a vortex core composed gas only. These velocity vectors were kept for the analysis and not filtered as being spurious during the post processing of the raw PIV data. It should be noted in Fig. 11 that for the quasi-flat free surface obtained at 100 RPM, only the highest row of vectors, just above the free surface, are spurious and are caused by small fluctuations of the interface location. The high radial velocity component close to the vessel axis was also noted for other PIV measurements carried out at a higher rotation speed with a very high free surface deformation. For example, at 275 RPM the air bubbles introduced in the vessel formed a gas column linking the agitator region and the free surface (Torré et al., 2007b). At this rotation speed it was noted that the experimentally measured radial velocity component was very high near the vessel axis.

Fig. 13 presents normalised axial and axial–radial velocity contour plots for the 200 RPM case and shows good agreement between the experimental data and the numerical predictions. The areas of low velocity which result from the creation of trailing vortices due to the impact of the fluid in tangential motion with the baffles appears clearly in Figs. 13(c) and (d).

## 5. Concluding remarks

A CFD model that can be used to perform transient simulations in partially baffled mixing vessels with free surfaces has been described. In previous papers (Torré et al. 2007a, b), the authors have demonstrated that this method provides good results in steady-state, transient mode and even with a non-constant agitator speed during agitator stopping. Here we show that at low rotation rates a steady, multiphase simulation does not converge, but it can be used as a starting point to obtain transient-averaged data from a converged transient simulation that agree reasonably well with the experimental data. An important result is that the system requires simulation of at least five impeller rotations to break down the initial flow pattern and meaningful averaging can only begin after around 15 revolutions. The time averages show a similar flow structure to the steady-state results but highlight a complex vortical motion with a period of just over two impeller revolution times. The transient model also captures the free surface behaviour well, as the steady-state model does at higher rotation speeds.

The current work compares numerical results obtained using the standard  $k-\varepsilon$  and the SSG Reynolds Stress turbulence models with experimental PIV data. The numerical predictions using the standard  $k-\varepsilon$  turbulence model show good agreement with experimental data. Surprisingly, the SSG Reynolds Stress

model, which is known to perform better than the  $k-\varepsilon$  for high swirling flows, gave unphysical results for axial velocities in the areas close to the vessel axis. Thus, the  $k-\varepsilon$  model was preferred to the RSM-SSG model for the multiphase simulations.

The power consumption has been determined both experimentally and numerically for different agitator rotation speeds. The power number was observed to decrease with Reynolds number at high Reynolds number, with this decreases being attributed to vortex formation and vessel aeration. Good agreement was obtained between the experimental value ( $N_p^{\text{exp}} = 1.85 \pm 0.4$ ) and numerical predictions ( $N_p^{\text{CFD}} = 1.6 \pm 0.1$ ).

The inhomogeneous multiphase model gives the same good agreement with experimental data as that from single phase simulations. The free surface was predicted to be quasi-flat at 100 RPM in agreement with experimental data. The multiphase simulations successfully reproduced the hydrodynamics and free surface shape for a case at higher rotation speed (200 RPM), where the free surface deformation cannot be neglected. More generally, the inhomogeneous multiphase approach used here for modelling a partially baffled vessel with a free surface, shows promise for the computation of hydrodynamics in other stirred vessels which have non-negligible free surface shape deformation. This method remains numerically affordable and allows the numerical assumption of a flat free surface, often made in computational studies, to be relaxed.

The major outstanding issue from this study is the inability of RANS turbulence models to capture the details of the precessing vortices seen experimentally. Such features could be studied using traditional LES simulation, which is extremely computationally expensive if it is applied throughout the flow domain) or more likely using Detached Eddy Simulation (DES) or Scale Adaptive Simulation (SAS) which retain the benefits of RANS simulations in boundary layers (where these models perform well), yet capture the turbulence structure in the bulk of the tank.

## Notation

$B'$	distance baffle-reactor, mm
$B_l$	baffles length, mm
$B_t$	baffle thickness, mm
$B_w$	baffle width, mm
$b_{ij}$	Reynolds stress anisotropy tensor in the SSG model
$C$	agitator clearance, mm
$C_D$	drag coefficient, dimensionless
$D$	agitator diameter, mm
$d_b$	bubble diameter, mm
$f_s$	FFT sampling frequency, Hz
$\mathbf{g}$	gravity acceleration, $\text{m s}^{-2}$
$H_d$	bottom dish height, mm
$H_{liq}$	liquid height, mm
$H_{\text{max}}$	maximum tank height, mm
$H_{PIV,\text{min}}$	bottom height of the PIV plane, mm
$H_{PIV,\text{max}}$	top height of the PIV plane, mm
$k$	turbulent kinetic energy, $\text{m}^2 \text{s}^{-2}$

$N$	agitator rotation speed, RPM, $s^{-1}$
$N_r$	number of agitator revolutions, dimensionless
$N_p$	agitator power number ( $=P/(\rho N^3 D^5)$ ), dimensionless
$n_b$	number of agitator blades, dimensionless
$n_B$	number of baffles, dimensionless
$P$	shear production term, $kg\ m^{-1}\ s^{-3}$
$\tilde{P}$	turbulence energy production, $kg\ m^{-1}\ s^{-3}$
$p$	pressure, Pa
$p', p''$	modified pressure, Pa
$r$	radial coordinate
Re	Reynolds number ( $=\rho N D^2/\mu$ ), dimensionless
$S_{ij}$	mean rate of strain tensor in the SSG model
$T$	tank diameter, mm
$T_0$	impeller torque, Nm
$t$	time, s
$t_b$	agitator blade thickness, mm
$U_a$	axial velocity, $m\ s^{-1}$
$U_r$	radial velocity, $m\ s^{-1}$
$U_a^*$	normalised axial velocity ( $=U_a/U_{tip}$ ), dimensionless
$U_{ar}$	axial–radial velocity, $m\ s^{-1}$
$U_{ar}^*$	normalised axial–radial velocity ( $=(U_a^2 + U_r^2)^{0.5}/U_{tip}$ ), dimensionless
$U_{tip}$	impeller tip velocity ( $=\pi N D$ ), $m\ s^{-1}$
$\mathbf{u}$	velocity, $m\ s^{-1}$
$u'$	velocity fluctuation, $m\ s^{-1}$
$w_b$	agitator blade width, mm
$Y$	axial coordinate
$W_{ij}$	mean vorticity tensor in the SSG model
$Z_{FFT}$	number of samples collected for the FFT

#### Greek letters

$\varepsilon$	dissipation rate of turbulent energy per unit volume, $m^2\ s^{-3}$
$\theta$	agitator retreat angle, degrees
$\mu$	dynamic viscosity, $kg\ m^{-1}\ s^{-1}$
$\rho$	density, $kg\ m^{-3}$
$\sigma$	power number standard deviation, Nm
$\phi_{ij}$	pressure–strain correlation in the SSG model, $kg\ m^{-1}\ s^{-3}$

#### Superscripts

CFD	numerical
eff	effective
exp	experimental
lam	laminar
T	matrix transposition
turb	turbulent

#### Acknowledgements

Tessenderlo Group and ANRT are acknowledged for financial support. The authors are indebted to the technical staff

of the LGC of Toulouse and particularly to A. Muller and J. Labadie. Special acknowledgement is given to D. Plotton and I. Touche for the excellent computer assistance they gave during this study.

#### Appendix A. Governing equations for the single phase simulations

After averaging and selecting a closure hypothesis, the Reynolds-averaged equations, called URANS (Unsteady Reynolds Averaged Navier–Stokes equations), are obtained. For clarity in the equations, the bar which represents averaged quantities is dropped, except for products of fluctuating quantities.

The continuity equation is expressed in Eq. (1) by

$$\nabla \cdot \mathbf{u} = 0 \quad (1)$$

##### A.1. $k$ - $\varepsilon$ model

As the standard  $k$ - $\varepsilon$  model employs the eddy-viscosity hypothesis, the momentum equation may be expressed as

$$\frac{\partial(\rho \mathbf{u})}{\partial t} + \nabla \cdot (\rho \mathbf{u} \otimes \mathbf{u}) = -\nabla p' + \nabla \cdot [\mu^{\text{eff}} (\nabla \mathbf{u} + (\nabla \mathbf{u})^T)], \quad (2)$$

where  $\mu^{\text{eff}}$  is the effective viscosity defined by

$$\mu^{\text{eff}} = \mu^{\text{lam}} + \mu^{\text{turb}} \quad \text{with} \quad \mu^{\text{turb}} = \rho C_\mu \frac{k^2}{\varepsilon} \quad \text{and} \quad C_\mu = 0.09,$$

$p'$  is a modified pressure expressed in Eq. (3) as

$$p' = p + \frac{2}{3} \rho k + \rho \mathbf{r} \cdot \mathbf{g}. \quad (3)$$

The values of  $k$  and  $\varepsilon$  come directly from the partial differential transport equations for the turbulent kinetic energy and the turbulence dissipation rate, which are expressed in Eqs. (4) and (5), respectively,

$$\frac{\partial(\rho k)}{\partial t} + \nabla \cdot (\rho \mathbf{u} k) = \nabla \cdot \left[ \left( \mu^{\text{lam}} + \frac{\mu^{\text{turb}}}{\sigma_k} \right) \nabla k \right] + \tilde{P} - \rho \varepsilon, \quad (4)$$

$$\frac{\partial(\rho \varepsilon)}{\partial t} + \nabla \cdot (\rho \mathbf{u} \varepsilon) = \nabla \cdot \left[ \left( \mu^{\text{lam}} + \frac{\mu^{\text{turb}}}{\sigma_\varepsilon} \right) \nabla \varepsilon \right] + \frac{\varepsilon}{k} (C_{\varepsilon 1} \tilde{P} - C_{\varepsilon 2} \rho \varepsilon), \quad (5)$$

with  $C_{\varepsilon 1}$ ,  $C_{\varepsilon 2}$ ,  $\sigma_k$  and  $\sigma_\varepsilon$  being model constants that are set to the usual values of 1.44, 1.92, 1.0 and 1.3, respectively.

The turbulence production due to shear is given as

$$\tilde{P} = \mu^{\text{turb}} \nabla \mathbf{u} \cdot (\nabla \mathbf{u} + (\nabla \mathbf{u})^T). \quad (6)$$

## A.2. Reynold stress model (SSG)

In the Reynolds Stress Model (RSM), the momentum equation to be solved is given by

$$\begin{aligned} \frac{\partial(\rho\mathbf{u})}{\partial t} + \nabla \cdot (\rho\mathbf{u} \otimes \mathbf{u}) \\ = -\nabla p'' - \nabla \cdot (\overline{\rho\mathbf{u}' \otimes \mathbf{u}'}) + \nabla \cdot (\mu\nabla\mathbf{u}), \end{aligned} \quad (7)$$

where  $p''$  is again a modified pressure. Unlike in the eddy viscosity model, the modified pressure has no turbulence contribution and is related to the static pressure by

$$p'' = p + \rho\mathbf{r} \cdot \mathbf{g}. \quad (8)$$

In this model separate equations are solved for the six components of the Reynolds stress tensor and for the turbulence energy dissipation rate ( $\varepsilon$ ). The anisotropic diffusion coefficients of the original models have been replaced by an isotropic formulation, which increases the robustness of the Reynolds stress model, as expressed in Eq. (9), written in Cartesian-tensor notation:

$$\begin{aligned} \frac{\partial(\overline{\rho u'_i u'_j})}{\partial t} + \frac{\partial(u_k \overline{\rho u'_i u'_j})}{\partial x_k} \\ = P_{ij} + \phi_{ij} + \frac{\partial}{\partial x_k} \left[ \left( \mu^{\text{lam}} + \frac{2}{3} C_S \rho \frac{k^2}{\varepsilon} \right) \frac{\partial \overline{u'_i u'_j}}{\partial x_k} \right] - \frac{2}{3} \delta_{ij} \rho \varepsilon, \end{aligned} \quad (9)$$

$\phi_{ij}$  is the pressure–strain correlation, and  $P_{ij}$  is the shear production term which is given by

$$\mathbf{P} = -\rho \overline{(\mathbf{u}' \otimes \mathbf{u}') (\nabla \mathbf{u})}^T + (\nabla \mathbf{u}) \overline{\mathbf{u}' \otimes \mathbf{u}'}. \quad (10)$$

As noted above, an additional equation is solved for the turbulence energy dissipation rate as

$$\begin{aligned} \frac{\partial(\rho\varepsilon)}{\partial t} + \frac{\partial(\rho u_k \varepsilon)}{\partial x_k} = \frac{\varepsilon}{k} (C_{\varepsilon 1} \tilde{P} - C_{\varepsilon 2} \rho \varepsilon) \\ + \frac{\partial}{\partial x_k} \left[ \left( \mu^{\text{lam}} + \frac{\mu^{\text{turb}}}{\sigma_{\varepsilon RS}} \right) \frac{\partial \varepsilon}{\partial x_k} \right], \end{aligned} \quad (11)$$

where

$$\mu^{\text{turb}} = \rho C_{\mu RS} \frac{k^2}{\varepsilon} \quad (12)$$

and the turbulent kinetic energy comes directly from  $k = \frac{1}{2} \overline{u'_i u'_i}$ .

The complete pressure strain term can be modelled, after the application of various kinematical constraints (Basara and Younis, 1995), by the form

$$\begin{aligned} \phi_{ij} = - (C_{S1} \varepsilon + C_{R1} \tilde{P}) \rho b_{ij} - C_{S2} \rho \varepsilon \left( b_{ik} b_{ij} - \frac{1}{3} b_{mn} b_{mn} \delta_{ij} \right) \\ + [C_{R2} - C_{R3} (b_{mn} b_{mn})^{1/2}] \rho k S_{ij} \\ + C_{R4} \rho k \left( b_{ik} S_{jk} + b_{jk} S_{ik} - \frac{2}{3} b_{mn} S_{mn} \delta_{ij} \right) \\ + C_{R5} \rho k (b_{ik} W_{jk} + b_{jk} W_{ik}), \end{aligned} \quad (13)$$

Table 2

Constants used in the SSG Reynolds Stress model

$C_{\mu RS}$	$\sigma_{\varepsilon RS}$	$C_S$	$C_{\varepsilon 1}$	$C_{\varepsilon 2}$	$C_{S1}$
0.1	1.36	0.22	1.45	1.83	1.7
$C_{S2}$	$C_{r1}$	$C_{r2}$	$C_{r3}$	$C_{r4}$	$C_{r5}$
-1.05	0.9	0.8	0.65	0.625	0.2

where  $b_{ij}$ ,  $S_{ij}$  and  $W_{ij}$  are the Reynolds stress anisotropy, the mean rate of strain and the mean vorticity tensors defined, respectively, in Eqs. (14)–(16), as

$$b_{ij} = \frac{\overline{u'_i u'_j}}{k} - \frac{2}{3} \delta_{ij}, \quad (14)$$

$$S_{ij} = \frac{1}{2} \left( \frac{\partial u_i}{\partial x_j} - \frac{\partial u_j}{\partial x_i} \right), \quad (15)$$

$$W_{ij} = \frac{1}{2} \left( \frac{\partial u_i}{\partial x_j} + \frac{\partial u_j}{\partial x_i} \right), \quad (16)$$

and

$$\tilde{P} = \frac{1}{2} \text{trace}(\tilde{P}) = -\overline{\rho \mathbf{u}' \otimes \mathbf{u}'} \cdot \nabla \mathbf{u}. \quad (17)$$

The model coefficients have been calibrated for a number of simple homogeneous flows, details of which may be found in Abid and Speziale (1993) and Speziale et al. (1991). The reader is referred to Basara and Younis (1995) for further details. The values used for the model constants are listed in Table 2.

## References

- Abid, R., Speziale, C.G., 1993. Predicting equilibrium states with Reynolds stress closures in channel flow and homogeneous shear flow. *Physics of Fluids A* 5 (7), 1776–1782.
- Adrian, R.J., 1991. Particle imaging techniques for experimental fluid mechanics. *Annual Review of Fluid Mechanics* 23, 261–304.
- Alcama, R., Micale, G., Grisafi, F., Brucato, A., Ciofalo, M., 2005. Large-eddy simulation of turbulent flow in an unbaffled stirred tank driven by a Rushton turbine. *Chemical Engineering Science* 60 (8–9), 2303–2316.
- Armenante, P.M., Luo, C., Chou, C.C., Fort, I., Medek, J., 1997. Velocity profiles in a closed, unbaffled vessel: comparison between experimental LDV data and numerical CFD predictions. *Chemical Engineering Science* 52 (20), 3483–3492.
- Aubin, J., Fletcher, D.F., Xuereb, C., 2004. Modeling turbulent flow in stirred tanks with CFD: the influence of the modeling approach, turbulence model and numerical scheme. *Experimental Thermal and Fluid Science* 28 (5), 431–445.
- Basara, B., Younis, B.A., 1995. Assessment of the SSG pressure-strain model in two-dimensional turbulent separated flows. *Applied Scientific Research* 55 (1), 39–61.
- Brucato, A., Ciofalo, M., Grisafi, F., Micale, G., 1998. Numerical prediction of flow fields in baffled stirred vessels: a comparison of alternative modelling approaches. *Chemical Engineering Science* 53 (21), 3653–3684.
- Budwig, R., 1994. Refractive index matching methods for liquid flow investigations. *Experiments in Fluids* 17 (5), 350–355.
- Campolo, M., Paglianti, A., Soldati, A., 2002. Fluid dynamic efficiency and scale-up of a retreated blade impeller CSTR. *Industrial Engineering and Chemical Research* 41, 164–172.
- Ciofalo, M., Brucato, A., Grisafi, F., Torraca, N., 1996. Turbulent flow in closed and free-surface unbaffled tanks stirred by radial impellers. *Chemical Engineering Science* 51 (14), 3557–3573.

- Ducci, A., Yianneskis, M., 2007. Vortex tracking and mixing enhancement in stirred processes. *A.I.Ch.E. Journal* 53 (2), 305–315.
- Duhamel, P., Vetterli, M., 1990. Fast Fourier transforms: a tutorial review and a state of the art. *Signal Processing* 19 (4), 259–299.
- Haque, J.N., Mahmud, T., Roberts, K.J., 2006. Modeling turbulent flow with free surface in unbaffled agitated vessels. *Industrial Engineering and Chemical Research* 45, 2881–2891.
- Hasal, P., Montes, J.L., Boisson, H.C., Fořt, I., 2000. Macro-instabilities of velocity field in stirred vessel: detection and analysis. *Chemical Engineering Science* 55 (2), 391–401.
- Hirt, C.W., Nichols, B.D., 1981. Volume of fluid (VOF) method for the dynamics of free boundaries. *Journal of Computational Physics* 39 (1), 201–225.
- Jaworski, Z., Zakrzewska, B., 2002. Modelling of the turbulent wall jet generated by a pitched blade turbine impeller—the effect of turbulence model. *Chemical Engineering Research and Design* 80 (A8), 846–854.
- Jaworski, Z., Dyster, K.N., Moore, I.P.T., Nienow, A.W., Wyszynski, M.L., 1997. The use of angle resolved LDA data to compare two different turbulence models applied to sliding mesh CFD flow simulations in a stirred tank. *Récents Progrès en Génie des Procédés* 11 (51), 187–194.
- Jenne, M., Reuss, M., 1999. A critical assessment on the use of  $k-\varepsilon$  turbulence models for simulation of the turbulent liquid flow induced by a Rushton-turbine in baffled stirred-tank reactors. *Chemical Engineering Science* 54 (17), 3921–3941.
- La Fontaine, R.F., Shepherd, I.C., 1996. Particle image velocimetry applied to a stirred vessel. *Experimental Thermal and Fluid Science* 12, 256–264.
- Lauder, B.E., Spalding, D.B., 1974. The numerical computation of turbulent flows. *Computational Methods Applied Mechanical Engineering* 3, 269–289.
- Li, M., White, G., Wilkinson, D., Roberts, K.J., 2004. LDA measurements and CFD modelling of a stirred vessel with a retreat curve impeller. *Industrial Engineering and Chemical Research* 43, 6534–6547.
- Li, M., White, G., Wilkinson, D., Roberts, K.J., 2005. Scale up study of retreat curve impeller stirred tanks using LDA measurements and CFD simulation. *Chemical Engineering Journal* 108 (1–2), 81–90.
- Mavros, P., 2001. Flow visualization in stirred vessels a review of experimental techniques. *Transactions of the Institute of Chemical Engineering* 79 (A), 113–127.
- Nagata, S., 1975. *Mixing: Principles and Applications*. Wiley, New York.
- Nikiforaki, L., Montante, G., Lee, K.C., Yianneskis, M., 2003. On the origin, frequency and magnitude of macro-instabilities of the flows in stirred vessels. *Chemical Engineering Science* 58 (13), 2937–2949.
- Nikiforaki, L., Yu, J., Baldi, S., Genenger, B., Lee, K.C., Durst, F., Yianneskis, M., 2004. On the variation of precessional flow instabilities with operational parameters in stirred vessels. *Chemical Engineering Journal* 102 (3), 217–231.
- Paglianti, A., Montante, G., Magelli, F., 2006. Novel experiments and a mechanistic model for macroinstabilities in stirred tanks. *A.I.Ch.E. Journal* 52 (2), 426–437.
- Paul, E.L., Atiemo-Obeng, V.A., Kresta, S.M., 2004. *Handbook of Industrial Mixing: Science and Practice*. Wiley, Hoboken, New Jersey.
- Roussinova, V., Kresta, S.M., Weetman, R., 2003. Low frequency macroinstabilities in a stirred tank: scale-up and prediction based on large eddy simulations. *Chemical Engineering Science* 58 (11), 2297–2311.
- Serra, A., Campolo, M., Soldati, A., 2001. Time-dependent finite-volume simulation of the turbulent flow in a free-surface CSTR. *Chemical Engineering Science* 56 (8), 2715–2720.
- Speziale, C.G., Sarkar, S., Gatski, T.B., 1991. Modelling the pressure–strain correlation of turbulence: an invariant dynamical systems approach. *Journal of Fluid Mechanics* 277, 245–272.
- Torré, J.P., Fletcher, D.F., Lasuye, T., Xuereb, C., 2007a. An experimental and computational study of the vortex shape in a partially baffled agitated vessel. *Chemical Engineering Science* 62 (7), 1915–1926.
- Torré, J.P., Fletcher, D.F., Lasuye, T., Xuereb, C., 2007b. Transient hydrodynamics and free surface capture of an under-baffled stirred tank during stopping. *Chemical Engineering Research and Design* 85 (A5), 626–636.
- Van den Akker, H.E.A., 2006. The details of the turbulent mixing process and their simulation. *Advances in Chemical Engineering* 31, 151–229.
- Verschuren, I., Wijers, J., Keurentjes, J., 2000. Mixing with a Pfaudler type impeller: the effect of micromixing on reaction selectivity in the production of fine chemicals. *Proceedings of the 10th European Conference on Mixing*, July 2–5, Delft, The Netherlands, pp. 69–75.
- Willert, C.E., Gharib, M., 1991. Digital particle velocimetry. *Experiments in Fluids* 10, 181–193.